Tectonic stress changes related to plate spreading prior to the 2021 Fagradalsfjall eruption in SW Iceland

Pavla Hrubcová [*], Václav Vavryčuk

Institute of Geophysics, Czech Academy of Sciences, Prague 4, Czech Republic

ABSTRACT

The Reykjanes Peninsula in SW Iceland is a part of the Mid-Atlantic plate boundary. It forms its transtensional segment with several volcanic and faulting systems. We focus on the 2017 seismicity that occurred in the central part of Reykjanes at the place of the Fagradalsfjall volcano prior to its eruption on March 19, 2021. We invert well-determined focal mechanisms of the 2017 seismicity and provide mapping of tectonic stress in space and time. Our results disclose heterogeneous stress field manifested by mix of shear, tensile and compressive fracturing. The prominent stress direction was in the azimuth of $120° ± 8°$, which represents the overall extension related to rifting in the Reykjanes Peninsula. The activity initiated on the transform fault segment with predominantly shear strike-slip events. The non-shear fractures occurred later being associated with normal dip-slips and corresponding to the opening of volcanic fissures trending in the azimuth of $30–35°$, perpendicular to the extension. The dip-slips were mainly located above an aseismic dike detected in the centre of the 2017 swarm. This dike represents a zone of crustal weakening during a preparatory phase of the future 2021 Fagradalsfjall volcanic eruption located at the same place. Moreover, we detected local variation of stress when the stress axes abruptly interchanged their directions in the individual stress domains. These stress changes are interpreted in a consequence of plate spreading and upcoming fluid flow during a preparatory phase of a rifting episode.

1. Introduction

Iceland is situated astride divergent Mid-Atlantic plate boundary separating the North American and Eurasian plates. It is the only section of the Mid-Atlantic Ridge exposed above sea level and it gives the unique opportunity to study divergent boundary onshore. It is located at the junction between the Reykjanes Ridge in the south (Martinez et al., 2020) and the Kolbeinsey Ridge in the north, the mid-ocean ridge segments nearest to Iceland. In-between these segments, the plate boundary is expressed at the surface by narrow belts of active faulting and volcanism bending across Iceland (Fig. 1). General spreading in Iceland is governed by movements of the two major lithospheric plates in the direction of 105°E with the spreading rate of ~19 mm/yr (Sigmundsson et al., 2020), confirmed by several models derived from geological, geophysical, and geodetic datasets (DeMets et al., 1994, 2010; Sella et al., 2002; Argus et al., 2010).

The Reykjanes Peninsula (RP) in the SW Iceland forms the transtensional plate-boundary segment with several volcanic and faulting systems. This zone comprises series of NE-SW trending volcanic fissures

parallel to a large number of NE-SW extensional normal faults, complemented by N-S strike-slips crosscutting the normal faults and fissures (Clifton and Kattenhorn, 2006; Thordarson and Larsen, 2007). The volcanic fissures trend ~30–40°E and extend several kilometres on both sides from the plate boundary zone. The fissures and faults form volcano-tectonic segments named after related geothermal fields (Einarsson, 2008; Einarsson et al., 2018), where both the mainshock-aftershock sequences and the earthquake swarms are observed (Keiding et al., 2009). The mainshock-aftershock sequences occur predominantly in the east of the Reykjanes Peninsula, while the earthquake swarms occur in the west.

The seismic activity in the Reykjanes Peninsula is high with periodicity every 20–40 years (Einarsson, 1991; Björnsson et al., 2020). The individual swarms are fast, typically lasting only few days, and then gradually terminating. The largest earthquakes ($M_L < 6$) are documented by right-lateral strike-slips along the N-S trending faults detected at the surface (Einarsson, 1991; Keiding et al., 2009; Fischer et al., 2022; Einarsson et al., 2023); the smaller earthquakes are characterized by a superposition of left-lateral shear and extension (Keiding et al.,

---

* Corresponding author.
E-mail address: pavla@ig.cas.cz (P. Hrubcová).

2008). In the central part of the peninsula, the seismicity is mainly localized within two volcanic fissures of Fagradalsfjall and Krýsuvík. It forms spatially dense earthquake clusters with a low background seismicity. The events are shallow, typically among 2–6 km depths (occasionally down to 13 km) and relate to a large number of faults and volcanic fissures (Keiding et al., 2009). Recent active periods were during 1929–1935, 1967–1973, 1997–2006 and continue to present.

In this paper, we focus on the 2017 swarm activity located at the place of the Fagradalsfjall 2021 eruption, which was recorded by broadband stations of local network REYKJANET (Horálek, 2013). From their recordings, we calculate accurate focal mechanisms and invert them for tectonic stress. We interpret this stress and provide its spatio-temporal analysis. Since the 2017 activity encompasses an aseismic dike directly at the place of the future 2021 volcanic eruption (Hrubcová et al., 2021; Fischer et al., 2022), we study local stress changes around this dike. Such an analysis sheds light on the links between magmatic and seismic processes and relates them to the active tectonic plate spreading prior to the eruption. The understanding of these processes contributes to mitigation of seismic and volcanic hazards at a divergent boundary.

2. Tectonic setting and tectonic stress

The Mid-Atlantic rift is identified by epicentres of earthquakes and shows a narrow zone of deformation (Fig. 1). In Iceland, it forms the accretionary plate boundary comprising en echelon stepping segments dominated by various volcano-tectonic systems (Thordarson and Larsen, 2007). Such a setting results from the interaction between the Mid-Atlantic rifting and the Icelandic mantle plume (Einarsson, 2008), though some authors speculate about the plume origin (Foulger and Anderson, 2005; Foulger, 2006; Foulger et al., 2020, 2021). Some segments are purely divergent expressed by normal faulting and fissuring as the Northern Volcanic Zone or two sub-parallel Western and Eastern Volcanic Zones. Some segments are expressed by transform tectonics dominated by strike-slip faulting with little volcanism as in the South Iceland Seismic Zone where the motion is interpreted by bookshelf faulting (Einarsson, 1991; Sigmundsson et al., 1995; Green et al., 2014). The Reykjanes Peninsula (RP) in the SW Iceland is expressed by transtensional tectonics with both volcanism and strike-slip movements similarly to the Grímsey Oblique Rift in the north.

The bending of the divergent plate boundary and its segmentation strongly influence tectonic stress, which reveal local variations in paleo and present-day regimes (Gudmundsson et al., 1996; Angelier et al., 2004, 2008; Plateaux et al., 2012; Hensch et al., 2016). The local stress field around Iceland is also influenced by interactions between volcanic and tectonic processes (Gudmundsson, 2006; Andrew and Gudmundsson, 2008). Ziegler et al. (2016) compiled present-day stress data and inverted earthquake focal mechanisms, geological fault slips and borehole stress indicators for the maximum horizontal compressive stress (Shmax). They determined four distinct domains with the Shmax rotating from the NE-SW direction in the Reykjanes Peninsula in SW, through NNE-SSW direction in central Iceland (at the transition from the North Volcanic Zone to the East Volcanic Zone), to the NNW-SSE direction in the north. In west Iceland, far away from the ridge, the Shmax rotates to the NW-SE direction being sub-parallel to the global plate motion. The rotation of the stress within Iceland is also evidenced by a spatial variation of the orientation of volcanic fissures, observed particularly near volcanoes (Hjartardóttir et al., 2012, 2016; Ziegler et al., 2016). They represent systems of tensile cracks, perpendicular to the minimum compressive horizontal stress (Shmin) or equivalently, to the maximum extensive stress.

The Reykjanes Peninsula (Fig. 2) represents an oblique spreading segment active during the last 6–7 million years, which is expressed by a 5–10 km wide and 60-km long seismic and volcanic zone. It strikes 70–80°E and connects the offshore Reykjanes Ridge in the west with the Western Volcanic Zone and the South Iceland Seismic Zone at the
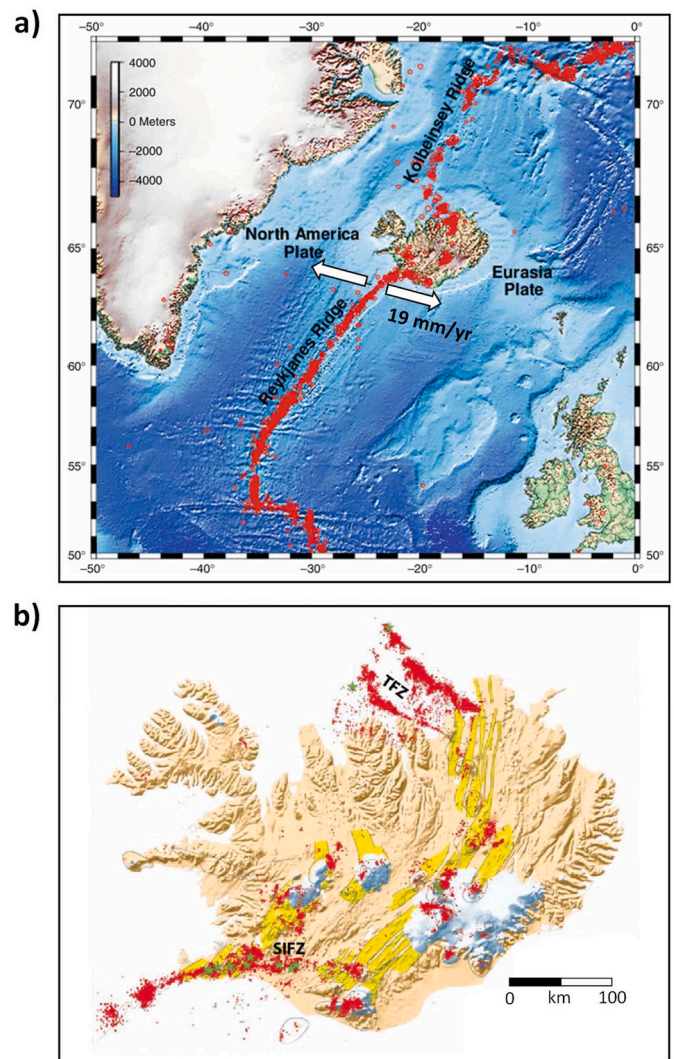
Fig. 1. (a) The 1964–2004 seismicity along the Mid-Atlantic Ridge system according to the International Seismological Centre (after Einarsson, 2015); (b) the 1994–2007 seismicity in Iceland located by the regional seismic network (after Jakobsdóttir, 2008).

Hengill triple junction in the east (Einarsson, 2008; Keiding et al., 2009). Such a setting produces transtensional tectonics with high seismicity, intense volcanism and high-temperature geothermal fields (Einarsson, 2008; Einarsson et al., 2018). The obliquity of the plate boundary, firstly observed geodetically, results in the left-lateral shearing combined with the extension along the NE-SW trending zones (Brander et al., 1976; Keiding et al., 2008). The NE-SW volcanic zones represent the main tectonic features on the Reykjanes Peninsula with hyaloclastite ridges and eruptive fissures, together with normal faults crosscut by a number of near-vertical N-S strike-slip faults mapped at the surface (Clifton and Kattenhorn, 2006; Einarsson et al., 2023). The largest earthquakes are associated with faulting along the N-S faults (Björnsson et al., 2020), and as in the South Iceland Seismic Zone, they resemble the bookshelf faulting (Hensch et al., 2016).

Tectonic stress derived from the inversion of focal mechanisms of local earthquakes in the Reykjanes Peninsula (Fig. 3) shows the Shmin direction of 120° ± 6°E (Keiding et al., 2009). This agrees with the direction of the maximum extensional strain rate derived from GPS measurements (Keiding et al., 2008) and complies with the results from detailed GPS data provided by Árnadóttir et al. (2009). The agreement between the direction of strain rate at the surface and stress at depth indicates that the seismicity is primarily driven by plate motion. This is
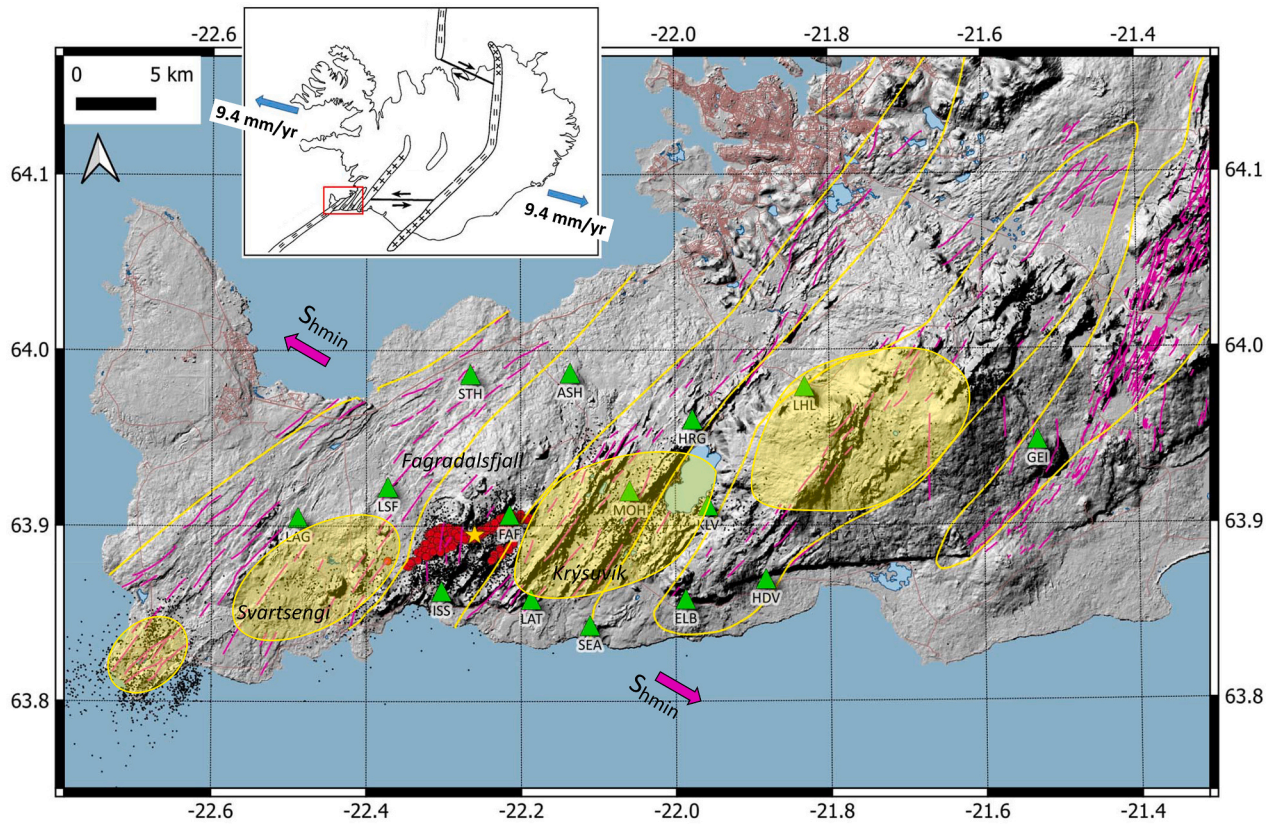
Fig. 2. The Reykjanes Peninsula in SW Iceland with the volcano-tectonic Fagradalsfjall segment, showing the transtensional part of the North Atlantic rift zone onshore. The double-difference locations of the 2017 seismic swarm (red circles) monitored by the REYKJANET network stations (green triangles). The black dots mark background seismicity located from the SIL network in the period of 2013–2019. The yellow star marks the Fagradalsfjall volcanic eruption on March 19, 2021. The violet lines indicate the faults detected at the surface (after Clifton and Kattenhorn, 2006); light yellow ovals indicate HT geothermal fields; yellow lines indicate volcanic systems. The violet arrows denote the Shmin at the Reykjanes Peninsula (Keiding et al., 2009; Ziegler et al., 2016). The inset shows active seismo-volcanic zones of Iceland (after Gudmundsson, 2000); the red rectangle indicates the area zoomed in the main map. Note the deviation between the direction of the global plate spreading of 105°E (blue arrows in inset) and the rotated local stress regime in the Reykjanes Peninsula with the Shmin direction of 120°E (violet arrows). (For interpretation of the references to colour in this figure legend, the reader is referred to the web version of this article.)
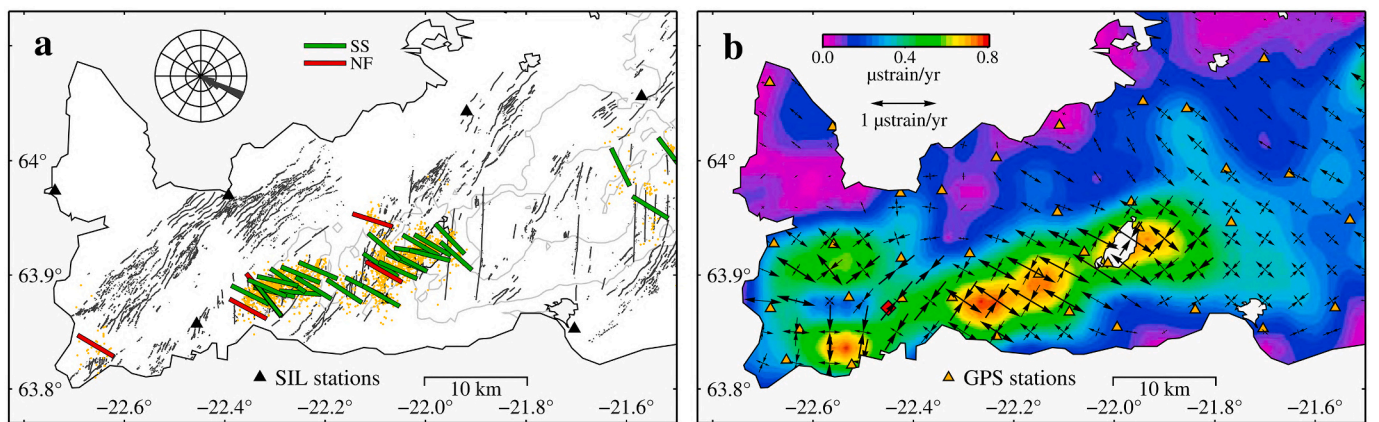

Fig. 3. (a) Estimated directions of Shmin from the stress inversions of 2000–2006 earthquake (yellow dots) focal mechanisms. The bars are coloured according to stress state: strike slip (green) and normal (red). The inset rose diagram shows the directions of Shmin. (b) Geodetic strain rates computed from 2000 to 2006 GPS velocities. The arrows show the greatest extensional and contractional horizontal strain rates; the magnitude of the maximum horizontal shear strain rate is indicated by colour (after Keiding et al., 2009). (For interpretation of the references to colour in this figure legend, the reader is referred to the web version of this article.)

also supported by the calculated moment released from the earthquakes and estimated moment from the plate motion (Keiding et al., 2009), though fluids can act as a secondary triggering mechanism.

3. Data

3.1. Earthquake swarm in 2017

The 2017 seismic swarm occurred in the Fagradalsfjall volcano-tectonic segment at the end of July 2017. The earthquakes reached local magnitudes $M_L < 3.7$ calculated with the formula for the Reykjanes Peninsula (Jakoubková, 2018). The seismicity consisted of >2000 earthquakes with $M_L > 0$. Their foci formed a focused cluster with seismic energy mostly released during the first three days (26–28 July 2017); however, a weaker seismicity continued until August 2017 (Fig. 4). The seismicity was recorded by local REYKJANET network stations (Horálek, 2013). Based on manual picking of the P- and S-wave onsets, it was located using the NonLinLoc algorithm (Lomax et al., 2009) in the 1D layered velocity model (SIL model) of Bjarnason et al. (1993). A 3D velocity model (Růžek, personal communications) was not applied since it was effectively within the resolution of the 1D-model locations with small hypocentre shifts of ~150 m in horizontal and ~100 m in depth directions.

Next, the earthquake locations were determined with a relative accuracy of ~100 m employing the relative double-difference location method (Waldhauser and Ellsworth, 2000) in the same velocity model. During the relocation, the sum of residuals decreased by 65% to 25 ms (see, Fischer et al., 2022). The resulting 9-km-long cluster of foci directed WSW-ENE with a strike of 67° in a depth range of 2–6 km (Fig. 5). It indicated two steep fault segments with a dip of ~85° in the east and a dip of ~70° in the west (Movie S1). From the spatiotemporal point of view, the seismicity migrated along the fault segments from east to west. In the central part of the fault zone, an aseismic gap at depths of 3–6 km was identified suggesting a deeper-seated ductile magmatic dike (see also Hrubcová et al., 2021). A few events located southerly were parallel with the main 2017 fault zone and coincided with the 2019 swarm activity delimiting together the plate boundary zone few kilometres thick (see also Fischer et al., 2022).

3.2. Focal mechanisms and seismic moment tensors

The focal mechanisms and seismic moment tensors were calculated from seismic recordings of 15 broadband stations (Guralp CMG-3ESPC sensors) of the local REYKJANET network (Fig. 2) deployed in 2013 (Horálek, 2013). The recordings were continuous, sampled by 250 Hz with a GPS timestamp; the epicentral distance of stations from the 2017 swarm foci was <20 km. The P- and S-wave automatic detections were refined manually to precisely identify the P- and S-wave onsets. To overcome seismic noise and obtain reliable solutions, the analysed earthquakes were limited by a local magnitude $M_L > 1$, which resulted in 389 double-difference located events ready for further processing.

We calculated seismic moment tensors (MTs) from the P-wave amplitudes observed at the vertical component of the velocity records (Davi et al., 2013; Davi and Vavryčuk, 2012; Vavryčuk et al., 2013; Yu et al., 2018). The P-wave amplitudes at stations were determined by the principal component analysis (Leaney, 2014; Vavryčuk et al., 2017), where the coefficients of the first principal component represented the effective amplitudes (including polarities) of the P wave at each station. The retrieved amplitudes were inverted for the full MTs. Since the waveforms were cross-correlated prior to the principal component analysis, the MT inversion was less sensitive to mislocations and to inaccuracy of the velocity model. The stability of the MT inversion was
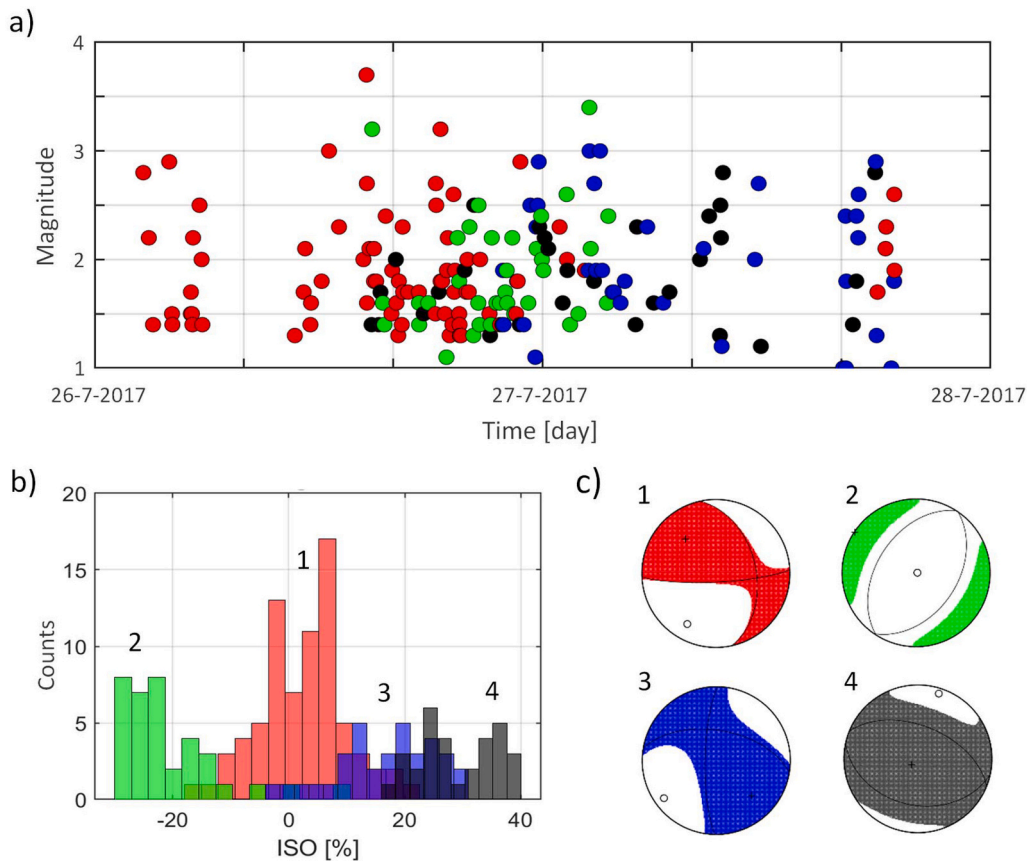

Fig. 4. (a) The magnitude-time plot with temporal evolution of the swarm. (b) The distribution of the volumetric (ISO) component of MTs of 182 events in the 2017 swarm. (c) Typical focal mechanisms colour-coded according to four retrieved clusters.
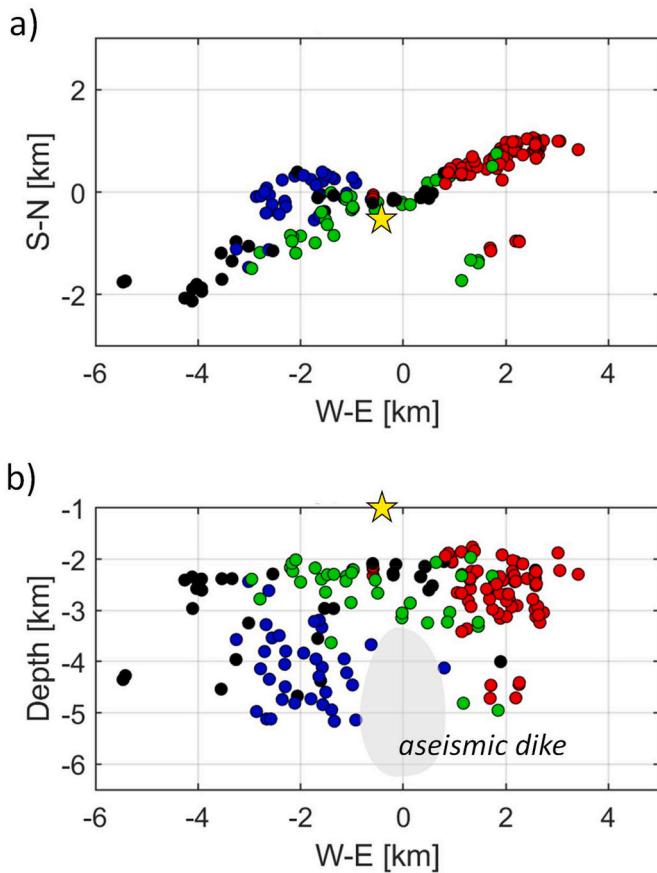
Fig. 5. The distribution of the most accurate 182 events in the 2017 swarm colour-coded according to four retrieved clusters (see Fig. 4c). (a) Horizontal section and (b) vertical section with events. The yellow star indicates the position of the 2021 Fagradalsfjall eruption. (For interpretation of the references to colour in this figure legend, the reader is referred to the web version of this article.)

assessed by numerical tests with waveforms contaminated by random noise and inverted repeatedly under the control by the root-mean-squares (RMS) of differences between theoretical and observed amplitudes (Hrubcová et al., 2021). In this way, we calculated standard deviations of MTs, of the double-couple and non-double-couple components of MTs, and of the P/T axes after Vavryčuk et al. (2017). The velocity model needed for calculating the ray-theoretical Green's functions was obtained by smoothing of a layered model used for locating the foci (Bjarnason et al., 1993). The Q factor was assessed after Menke et al. (1995) and related to the reference frequency of 10 Hz corresponding to the prevailing P-wave frequency (see Hrubcová et al., 2021, Table 1).

The resulting MTs of 389 analysed events were checked for their accuracy in order to eliminate less-determined earthquakes with unfavourable station coverage or with waveforms distorted by non-modelled effects. We tested several criteria to assess the quality of

Table 1
Double-couple (DC) and volumetric (ISO) components of the typical (centroidal) MTs.

Cluster	Number of events	Strike [°]	Dip [°]	Rake [°]	DC [%]	ISO [%]
1	77	87.2	80.5	45.9	82.0	3.1
2	38	34.5	43.9	−88.7	50.5	−25.3
3	35	181.0	77.7	145.3	62.8	14.9
4	32	102.1	37.1	82.2	39.1	35.1

retrieved MTs; we aimed at stable and robust solutions consistent with the selection of Hrubcová et al. (2021). We applied following strict quality criteria: (i) the number of stations recording the events >10; (ii) the root-mean-square of the retrieved optimum MTs <0.15; (iii) the mean deviation of the P/T axes of MTs calculated from noisy and noise-free data <12°; and (iv) the standard deviation of the volumetric component percentage <12%. The standard errors in the P/T axes solutions were quantified from 100 repeated inversions of MTs contaminated by random noise with a noise level of 25% and they were typically 2° and 5° for the P and T axes, respectively. The application of these criteria enabled us to select 182 earthquakes with the most accurate MTs and to calculate their focal mechanisms (DC solutions) needed for the stress inversion. The original MTs of 389 analysed events were the same as discussed in Hrubcová et al. (2021); however, we limited our selection to 182 events with the most accurate MTs necessary for the spatiotemporal analysis of tectonic stress.

The fault plane solutions of the selected 182 events are presented in the form of the P/T axes composite plots (Fig. 6). The P/T axes form several well-separated clusters, which are mixed only in the near-vertical directions. The P axes are aligned along a SW-NE strip; the T axes are aligned in the NW-SE direction and correspond to the extension of the divergent plate boundary. Since the focal mechanisms are very accurate, the mix of the P/T axes in the near-vertical directions is not due to errors but it indicates a complicated spatiotemporal stress pattern.

4. Classification of focal mechanisms and their evolution in space and time

Hrubcová et al. (2021) interpreted seismicity in 2017 swarm and identified three distinct clusters of the P/T axes in the 2017 swarm. They considered this classification as an optimum with respect to their main target (the variations in volumetric components of MTs). However, they were aware of limitations and suggested a more detailed clustering in further interpretations. Here, we go beyond this analysis and reveal further well-nested, robust and stable phenomena in the focal zone. After testing, we concluded that four clusters of focal mechanisms optimally reflect a diversity of the fault segments and stress domains.

We applied the four-cluster classification with the k-means algorithm (Jain, 2010; Vavryčuk et al., 2017) and determined four clusters with typical (centroidal) moment tensors in each cluster. In this approach,
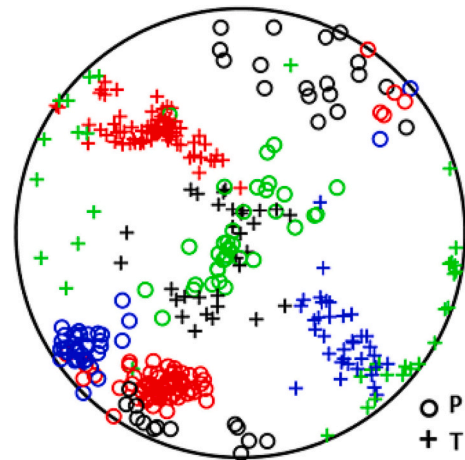

Fig. 6. The P/T axes of individual events. The colour coding is according to the typical (centroidal) focal mechanisms (see Fig. 4c). Note that both the P axes of green focal mechanisms and T axes of black focal mechanisms are nearly vertical. This is a clear indication that these earthquakes occurred under different stress regimes. (For interpretation of the references to colour in this figure legend, the reader is referred to the web version of this article.)

each cluster of MTs is defined by its centroid and the positions of centroids are found by minimizing the sum of distances of all full MTs (Willemann, 1993; Cesca et al., 2014; Vavryčuk et al., 2017). The number of clusters is the only parameter controlling the procedure. The clustering of the most reliable 182 events is recognized in space and time. Moreover, the earthquakes show four-cluster distribution of the non-DC volumetric components of MTs (Fig. 5), which corresponds to the distribution recognized by Hrubcová et al. (2021) for three clusters. These components contribute to understanding of processes related to stress redistribution and spreading.

The typical representative focal mechanisms in each cluster (Table 1) display the following properties:

(1) The first-type mechanism comprises the majority of events (Figs. 4 and 5, red colour) aligned along the WSW-ENE oriented plate boundary on the Reykjanes Peninsula (strike of ~80°) in a depth range of 2–6 km. The mechanism shows either the left-lateral strike-slip with a weak normal component or the N-S right-lateral strike-slip; and as expected for shearing, their volumetric components are close to zero. These events are located in the east, initiated the swarm activity and comprised the strongest M_L 3.7 event.

(2) The second-type mechanism (less numerous) is normal with the SW-NE (~35°) strike (Figs. 4 and 5, green colour). It occurs in the central part namely above the aseismic gap and comprises shallower events connecting the eastern and western fault segments. They exhibit the second highest magnitude M_L 3.4 and their volumetric components are negative. With the horizontal T axis in 305°, this mechanism relates to the extensional rifting in the azimuth of 120°/300° determined also by Keiding et al. (2009).

(3) The third-type mechanism exhibits the strike-slips with a shear motion both in N-S (strike 180°) and E-W (strike 280°) directions (Figs. 4 and 5, blue colour). These events have positive volumetric components and smaller magnitudes (M_L < 3). They are located in the western fault segment in a depth range of 2–5.5 km and terminated the swarm activity.

(4) The fourth-type events are reverse with the WNW-ESE strike (~105°) (Figs. 4 and 5, black colour). With the P axis in ~20° they are nearly perpendicular to the extension. They exhibit the most positive volumetric components and have the smallest magnitudes (M_L < 2.8). The events are shallow, located in the west and together with the other events in the west suggest later stages of activation.

The percentages of DC and ISO components of MTs were calculated according to the eqs. (6–10) of Vavryčuk (2015b).

5. Tectonic stress analysis

The stress field at seismogenic depths is commonly inverted from earthquake focal mechanisms under two basic assumptions. (1) The stress should be uniform within a given space and time period, for which the earthquakes respond to the stress field. (2) The focal mechanisms display a sufficient diversity, which must be of the physical origin (Vavryčuk, 2015a). If the above conditions are reasonably satisfied, we can invert four parameters. The inverted stress is characterized by three principal stress directions: σ_1, σ_2, and σ_3, representing the most compressive, intermediate, and the least compressive principal stresses, respectively (where the compression is positive and equals 1). They are supplemented by the stress ratio parameter $R = (\sigma_1 - \sigma_2) / (\sigma_1 - \sigma_3)$; $0 \leq R \leq 1$ (Vavryčuk, 2015a).

If the stress field is not homogeneous, the seismicity must be subdivided into domains in space and/or time where homogeneity is reasonably satisfied. Consequently, focal mechanisms of individual domains must be inverted separately. Remarkable stress inhomogeneities can be indicated, in particular, by a mix of completely different focal mechanisms with overlapping P and T axes or with focal mechanisms covering the whole variety of normal, reverse and strike-slip faulting. This is exactly observed in the 2017 seismicity (Fig. 6). Hence, focal mechanisms corresponding to individual stress domains must be effectively identified and separated by the cluster analysis. After that, the focal mechanisms of individual clusters can be inverted for stress in order to map the spatiotemporal variation of the stress field in the focal zone (Vavryčuk and Adamová, 2018; Vavryčuk et al., 2021).

The analysis of stress in different domains requires high-quality data constrained by strict quality criteria. Hrubcová et al. (2021) focused on well-determined MTs in the 2017 swarm and interpreted their non-DC volumetric components. These components revealed significant variations coinciding with spatial and temporal distributions of events along the fault as well as with systematic trends in the mechanism types. In their interpretation, Hrubcová et al. (2021) involved as many data as possible to show robust variations of the non-DC components. They eliminated problematic events with unfavourable station coverage or with amplitudes significantly distorted by unmodelled effects. However, they tried to preserve the highest possible number of events. They identified 251 MTs and divided them into three clusters with a distinctly different behaviour of the non-DC volumetric components.

Here, we applied stricter criteria for selecting the accurate MTs and analysed 182 events of the highest accuracy. Moreover, to preserve the condition of stress uniformity in each domain, we divided focal mechanisms into four clusters. Two clusters, i.e., the strike-slip mechanism 1 (Fig. 4c, red colour) and the normal mechanism 2 (Fig. 4c, green colour), were identical with the respective clusters of Hrubcová et al. (2021). However, their third cluster with positive volumetric components split into two additional clusters. These two clusters comprise the strike-slip mechanism 3 (Fig. 4c, blue colour) with slightly more oblique shearing compared to the mechanism 1, and the reverse focal mechanism 4 with the WNW-ESE strike (105°) (Fig. 4c, black colour); both of them characterized by high positive volumetric components of MTs (Fig. 4b). Though the latter mechanism is less frequent, it was also detected by Keiding et al. (2009), and represents a response to a pronounced heterogeneity necessary to consider when inverting for stress.

The stress inversion of the 2017 swarm was performed with the open-public Matlab code STRESSINVERSE (http://www.ig.cas.cz/stress-inverse) developed by Vavryčuk (2014), which jointly inverts focal mechanisms for stress and fault orientations. This method is based on the Michael's inversion scheme (Michael, 1984, 1987) but it is run in iterations. During the iterations, the fault instability criterion is applied for discriminating which of the nodal planes is the fault (Vavryčuk et al., 2013). The approach is fast, robust and provides uncertainty limits of the results.

Apart from the inversion for stress in each domain, we evaluated the faults and their liability to slip. The stability of a fault to sustain the stress can be conveyed by the Mohr-Coulomb failure criterion (Zoback, 2007), where the shear stress on the activated fault must exceed a critical value given by normal stress, pore pressure and fault rheology parameters (cohesion and friction). It can be displayed in the Mohr's circle diagram representing the relation between normal (σ) and shear (τ) stress components. The diagram also defines two principal focal mechanisms representing optimally oriented fault planes in respect to the tectonic stress regime (Vavryčuk, 2011). The active fault planes under given stress should not be too different from those of the principal focal mechanisms. Predominant faulting and its scatter are projected into a scatter of the P/T axes, which form clusters of a specific shape with a typical two-wing or butterfly-wing pattern. Each wing of the P/T

Table 2
Results of the stress inversion for individual stress domains.

Cluster	Number of events	σ_1 axis		σ_2 axis		σ_3 axis		Shmin	Shmax
		Az [°]	Pl [°]	Az [°]	Pl [°]	Az [°]	Pl [°]	[°]	[°]
1	77	210	17	99	49	313	36	123	33
2	38	85	82	216	5	307	6	128	38
3	35	236	13	355	65	141	21	145	55
4	32	22	11	113	2	214	78	112	22

Az – azimuth, Pl – plunge. Directions of the Shmin and Shmax were calculated according to Lund and Townend (2007).

axes on the focal sphere corresponds to the failure conditions in the upper and lower half-planes in the Mohr's circle diagram, respectively. The butterfly wings are well separated provided that friction is high (0.5 or higher); if friction is low, the wings come closer or they overlap (Vavryčuk, 2011).

5.1. Tectonic stress in individual domains

The stress analysis was performed for the focal mechanisms of 182 stable and accurate MTs divided into four clusters (Fig. 4c), where homogeneity of the stress in space and/or time was assumed. The well-

defined clustered P/T axes of events indicate homogeneity of the stress within individual domains. The resulting stress in each domain (Table 2) is depicted with confidence limits; the separation of the P/T axes together with the Mohr's diagram in each cluster indicate the friction. The stress in each domain showed the following results:

(1) The majority of events with the strike-slip mechanism 1 initiated the activity and showed the resultant principal stress directions (azimuth/plunge) $\sigma_1 = 210°/17°$, $\sigma_2 = 99°/49°$, and $\sigma_3 = 313°/36°$ (Fig. 7, first row, and Table 2). The stress ratio R is 0.65. The maximum compression axis σ_1 is nearly horizontal; the other
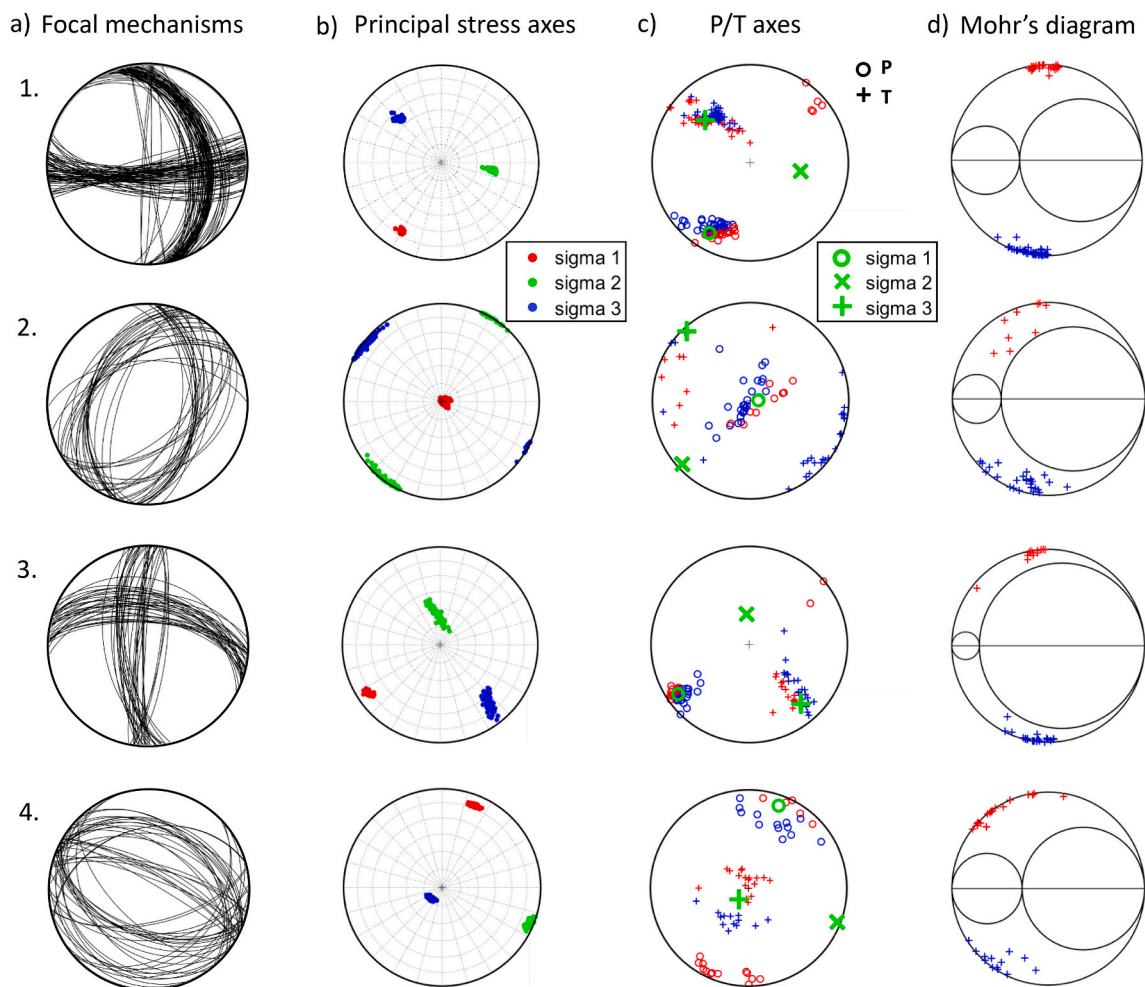

Fig. 7. The stress inversion of individual cluster sequences of the 2017 swarm. (a) The focal mechanisms in each cluster 1–4. (b) The principal stress axes σ_1, σ_2, and σ_3 with their confidence limits. (c) The P/T axes of individual earthquakes. The circles mark the P axes; the plus signs mark the T axes. The red and blue colours depict the faults symmetrically oriented with respect to the maximum compression. The principal stress axes are indicated in green. Note close or overlapping P/T axes in clusters 1, 2, and 3 indicating low friction; note well-separated P/T axes in cluster 4 indicating high friction. (d) The Mohr's diagrams with the upper and lower half-planes. Note low friction for clusters 1–3 (events close to the top and bottom of σ_1 circle); and higher friction for cluster 4 (events at the left of σ_1 circle). The red and blue colours in (c) and (d) denote respective events belonging to the same wings. (For interpretation of the references to colour in this figure legend, the reader is referred to the web version of this article.)

principal axes σ_2 and σ_3 are inclined. The σ_1 axis corresponds to the transform faulting; the σ_3 axis relates to the least compressive (i.e. the maximum extensive) horizontal stress. The Shmin is in 123°E in agreement with the extension in the Reykjanes Peninsula (Fig. 3). The prevailing mechanism is the N-S right-lateral oblique strike-slip, related to N-S trending faults mapped at the surface (Clifton and Kattenhorn, 2006) and detected for shearing for large earthquakes (Hensch et al., 2016; Björnsson et al., 2020; Fischer et al., 2022). It is complemented by left-lateral oblique strike-slip with the strike of 83° in agreement with the trend of the oblique plate boundary.

(2) By contrast, the stress inversion of the normal focal mechanism 2 yield quite different results. The stress inversion reveals the vertical σ_1 axis, with two horizontal axes σ_2 (azimuth 216°) and σ_3 (azimuth 307°), see Fig. 7 (second row) and Table 2. The stress ratio R is 0.69. The Shmin has an azimuth of 128°E, which is the stress direction that corresponds to the extension in the Reykjanes Peninsula detected by Keiding et al. (2009) (Fig. 3). It relates to rifting with the normal faults striking 35°E in agreement with the trend of volcanic fissures (Clifton and Kattenhorn, 2006; Thordarson and Larsen, 2007).

(3) The stress inversion of the strike-slip mechanism 3 exhibits a nearly horizontal σ_1 axis (azimuth 236°), nearly vertical σ_2 axis, and nearly horizontal σ_3 (azimuth 141°), see Fig. 7 (third row) and Table 2. The stress ratio R amounts 0.86. The faulting is represented by almost vertical shearing along the N-S and W-E trending faults. The Shmin has the azimuth of 145°E and is rotated by ~20–25° from the extension of $120 \pm 6°E$ reported by Keiding et al. (2009).

(4) The stress inversion of the reverse mechanism 4 shows both horizontal σ_1 (azimuth 22°) and σ_2 (azimuth 113°), with a nearly vertical σ_3 axis (azimuth 214°), see Fig. 7 (fourth row) and Table 2. The stress ratio R is 0.62. The Shmin has an azimuth of 112°E and is close to the extension of $120 \pm 6°E$ of Keiding et al. (2009).

The errors in the stress directions range between 5 and 15° (Fig. 7b). The instability analysis for all clusters and the distribution of events in the Mohr's circle diagrams indicate the majority of activated fractures well oriented for shearing. The red and blue plus signs in the upper and lower Mohr's circle diagram (Fig. 7d) depict the faults symmetrically oriented with respect to the maximum compression; the same distribution of faults is indicated in the P/T axes plot (Fig. 7c).

5.2. Tectonic stress changes in space and time

The spatiotemporal stress changes are imaged in Fig. 8. The gradually increased stress along the oblique plate boundary triggered the 2017 activity and activated predominantly shear earthquakes in the east (Figs. 4 and 5, red colour), which was optimally oriented for shearing and close to failure. The maximum compression axis was nearly horizontal; the other principal stress axes were inclined. Later, the predominant motion changed to a horizontal opening above the aseismic dike along the stress axis with the maximum extension/minimum compression (Figs. 4 and 5, green colour). The horizontal extension produced cracking and subsequent collapse of the uppermost layers just above and around the dike. The stress was released by shallow seismicity characterized by normal focal mechanisms (mechanism 2) with negative (compressional) volumetric components of MTs (Fig. 4b). These motions resulted in subsidence of the layers above the dike.

The redistribution of stress triggered the events in the west with positive volumetric components (Fig. 4b, blue and black colours). Such a fracturing mode with a significant tensile component can be explained by a subsequent escape of the over-pressurized fluids in the upward direction along newly formed cracks. The fluid flow initiated tensile cracking. Both maximum and minimum compression (mechanism 3) were horizontal (Fig. 8b, blue colour); however, the Shmin in the azimuth of ~145° was deviated with respect to the other stress domains (azimuth of $120° \pm 8°$) (Fig. 8a). This might indicate an inhomogeneity in the west. Finally, the high overpressure of fluids and their flow upwards to the surface caused local domination of vertical stress (Fig. 8a, black colour). Its magnitude even exceeded the magnitude of the regional maximum horizontal compressive stress. The associated focal mechanisms contained high positive volumetric components reflecting their tensile character (mechanism 4). Such a geometry is well known in the fluid-filled environments, for example in hydrofracture experiments, where tensile cracks along the maximum compression are formed by the injection of over-pressurized fluids into the rock (e.g., Boyd et al., 2018). The overall saturation of the crust by fluids escaping after the stress relaxation decreased the friction and helped the faults or cracks to fail (Vavryčuk and Hrubcová, 2017).
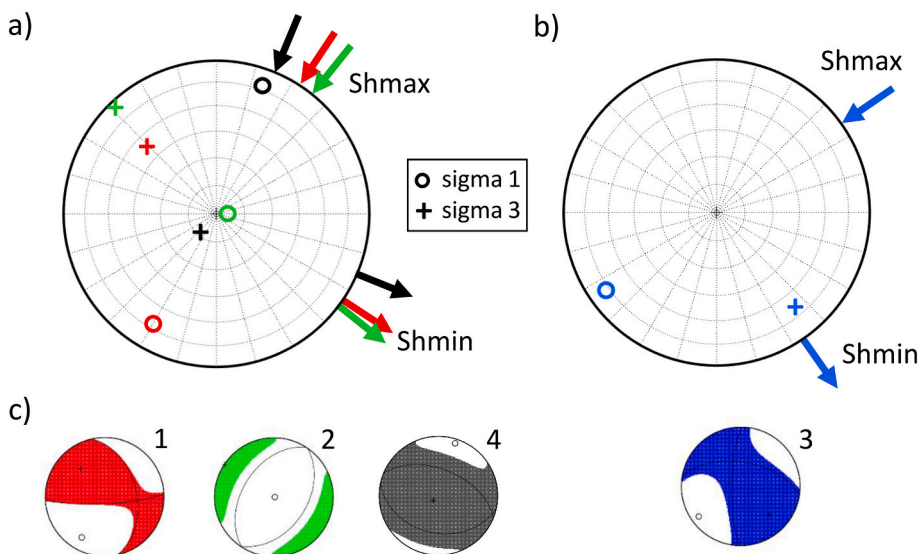

Fig. 8. The principal stress axes σ_1 (open circles) and σ_3 (plus signs) of clusters 1, 2, and 4 (a); and cluster 3 (b). The arrows indicate directions of horizontal stresses Shmax/Shmin in individual clusters. (c) The typical focal mechanisms in each cluster. Note: (i) similar Shmax and Shmin directions for clusters 1, 2, and 4, and anomalous direction in cluster 3, and (ii) the exchange of the maximum compression (green circle) and the maximum extension (black plus sign) in the vertical direction in clusters 2 (normal mechanism) and 4 (reverse mechanism) while keeping the other axes nearly horizontal.

The stress changes in the 2017 swarm reflect tectonic processes at the transtensional plate boundary. After the initial phase of activity in the east with predominantly shear earthquakes (mechanism 1), the earthquakes in later phases were characterized by normal/reversed focal mechanisms with compressive/tensile motions partially mixed in time (mechanisms 2 and 4). This is also in agreement with the later activation of shear-tensile events in the west (mechanism 3) showing positive volumetric components. This later stage was mostly associated with fluid flow from depth to the surface. Though these processes were fast, the earthquakes of different focal mechanisms formed clear spatial domains well separated from each other.

5.3. Fault plane orientation

The stress analysis helps to distinguish, which of the two nodal planes is the activated fault (Vavryčuk, 2011). In general, the highest probability of the fault to fail is associated with a fault plane optimally oriented in the stress field. Each stress field allows for the existence of two such fault planes, called principal, with two distinct principal focal mechanisms occurring along each plane (Vavryčuk, 2011). Their orientation depends on the stress and fault friction. The deviation of these principal fault planes from the σ_1 axis must be $<45°$; however, the optimally oriented planes are usually deviated by 30–35° from the σ_1 axis in the compressive environments (Vavryčuk et al., 2017).

In the Reykjanes Peninsula, the principal faults for the strike-slip earthquakes (mechanism 1) are in the azimuths of 75° and $-5°$ (Fig. 9) and are associated with the left-lateral oblique plate boundary

Fig. 9. (a) Tectonic scheme of the principal faults along the transtensional plate boundary at the Reykjanes Peninsula. (b) Two principal fault planes of the strike-slip mechanism 1. Note two principal faults corresponding to the left-lateral divergent plate boundary and the conjugate right-lateral N-S trending faults mapped at the surface. The grey bow ties depict the variety in the fault orientations.

complemented by the right-lateral N-S trending faults mapped at the surface. Both faults are optimally oriented for shearing with respect to the stress field. However, statistically, the N-S trending faults are activated in the majority of events and also for the largest events. The oblique plate boundary is a mature fault zone, most probably filled with fluids, and thus close to failure. As such, it cannot sustain high stress. The release of seismic energy is fast with smaller events. On the other hand, the right-lateral N-S trending faults are documented at the surface (Einarsson, 1991; Clifton and Kattenhorn, 2006; Einarsson et al., 2023) and by the strongest earthquakes (Hensch et al., 2016; Björnsson et al., 2020) including the M_L 5.3 in the 2021 swarm activity preceding the Fagradalsfjall eruption (Fischer et al., 2022). These faults are newly developed and can sustain higher stress. The release of seismic energy needs to overcome a barrier resulting in the formation of new faults and cracks (Vavryčuk and Adamová, 2018). For this reason, these faults are associated with the strongest earthquakes and also detected at the surface.

6. Discussion

The analysis of the 2017 swarm mapped stress changes in space and time (Fig. 7). The overall stress is both strike-slip and normal as reported by Keiding et al. (2009). Moreover, a detail analysis shows also strong local heterogeneities. They are manifested by the occurrence of distinctly different types of focal mechanisms characterized by shear, tensile and compressive fracturing. Although the fracturing regimes were diverse, the directions of the principal stress axes were stable (Fig. 8). Except for σ_2 and σ_3 of cluster 1 (Fig. 7, first row), they exhibited nearly vertical and/or nearly horizontal directions. The differences in the stress regimes thus originated in different magnitudes of the principal stresses rather than in the rotation of the principal stress coordinate system. Hence, the principal stress directions were essentially fixed in the focal zone, and the σ_1, σ_2 and σ_3 axes only switched their orientations in individual stress domains. The only rotation of the stress axes was detected for cluster 3, where the Shmin deviates by ~20–25° from the direction of the mean extension at ~120°.

Tectonically, the overall heterogeneity of the stress field is consistent with processes at the divergent plate margins and relates to the transtensional setting at the Reykjanes Peninsula (Fig. 10). The transform part of the oblique plate boundary is documented by the majority of strike-slip events (mechanism 1), which initiated the activity and shows the maximum compressive stress direction in the azimuth of 33°. The maximum compression axis σ_1 is nearly horizontal and corresponds to the transform faulting; the other principal axes σ_2 and σ_3 are inclined. The other oblique strike-slip mechanism (mechanism 3) contains a significant amount of the volumetric component and exhibits a nearly horizontal σ_1 axis. Its Shmin is clockwise rotated by ~20–25° (azimuth 145°) from the regional mean value of ~120°, which points to the complex stress conditions in deeper parts of the focal zone in the west (Fig. 10). This is also manifested by the distribution of foci with this mechanisms, which are aligned along more inclined fault (dipping ~70°) compared to the near vertical fault (dipping ~85°) in the east.

The tensile fractures are associated with normal dip-slips and correspond to the volcanic fissures in the azimuth of 30–35° (Fig. 9a). They are perpendicular to the local extension, which exhibits the most stable and prominent direction visible in clusters in the azimuth of Shmin 120° ± 8° (Table 2). This direction represents the overall extension related to rifting in the Reykjanes Peninsula (Fig. 10). The same azimuth of Shmin 120° ± 6° was reported by Keiding et al. (2009) from the stress inversion during 1997–2006 and is consistent with the GPS strain rate directions during 2000–2006 (Keiding et al., 2008) (Fig. 3). However, these Shmin values are different from global plate motion for the whole Iceland spreading in the direction of 105°E (Sigmundsson et al., 2020) derived from the NUVEL-1A plate model (DeMets et al., 1994). This discrepancy reflects the transtensional setting in the Reykjanes Peninsula, facing bending of the Mid-Atlantic rift in
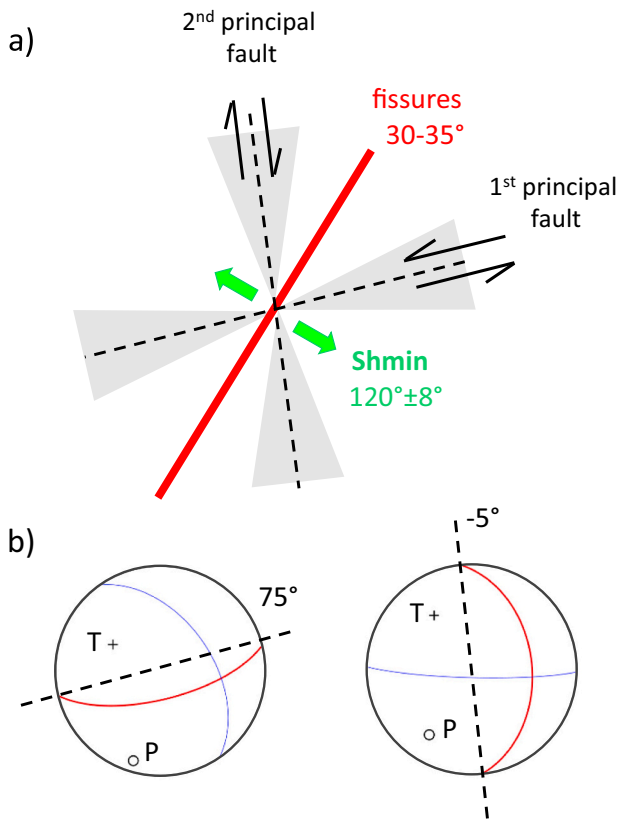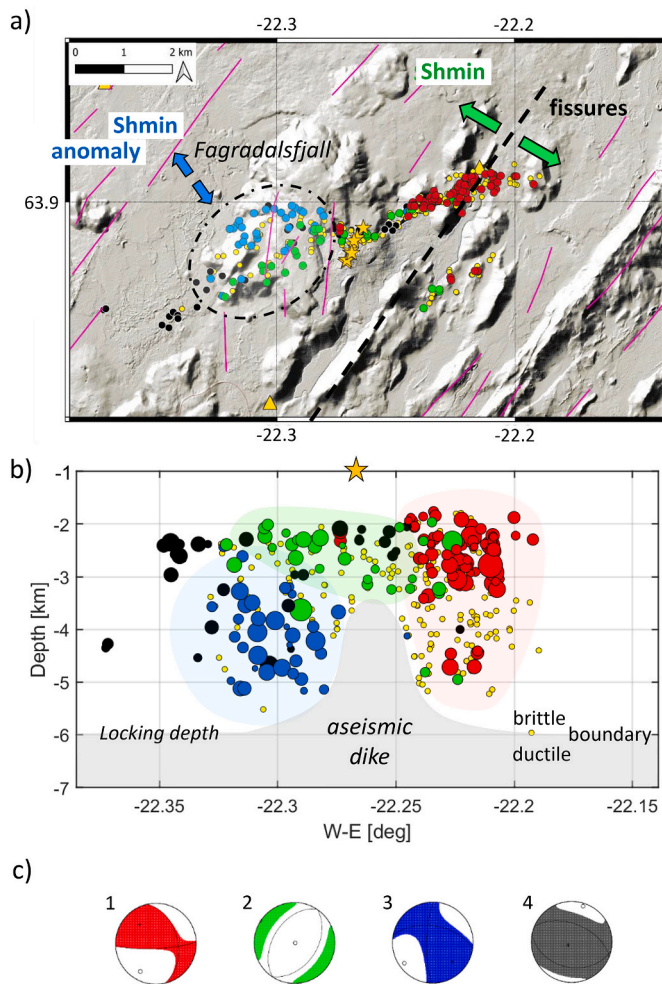
Fig. 10. The 2017 seismicity (yellow circles) with 182 events (colour-coded according to four clusters). (a) The map view with the minimum horizontal compressive stress direction Shmin (green arrows) related to the maximum extension. The ellipse marks the stress domain at depth with rotated Shmin (blue arrows). The violet lines represent detected faults at the surface (after Clifton and Kattenhorn, 2006). Note the trend of the tensile volcanic fissures perpendicular to Shmin. (b) The depth-section view with the magnitude indicated by size. (c) The typical (centroidal) focal mechanisms. The orange stars mark the Fagradalsfjall March 2021 volcanic eruption fissure above the aseismic dike. Note different regimes in different fault segments separated by the dike with the subsequent eruption. (For interpretation of the references to colour in this figure legend, the reader is referred to the web version of this article.)

response to the interaction with the Icelandic mantle plume (Einarsson, 2008).

The compressive fracturing is mainly located above the aseismic zone in the centre of the 2017 swarm (Fig. 10, green colour). The negative volumetric components of the dip-slip earthquakes (Fig. 4b, green colour) associated with collapses of the uppermost layers just above and around the dike indicate that the activity was not driven by magma upraise, where otherwise rather positive volumetric components would be anticipated. The aseismic dike thus represents a zone of crustal weakening during a preparation phase for future eruption. In such a case, magma plays rather passive role during the extension at the divergent plate boundary. This is also supported by the absence of crustal magma chamber and primitive lava of the Fagradalsfjall 2021 eruption dominated by melts sourced from the uppermost mantle (Halldórsson et al., 2022).

A combination of transform and tensional stresses in the 2017 pre-

eruption activity enabled transtensional faulting and led to the volcanic eruption in 2021. This is documented by switching the principal stress axes of normal and shear mechanisms (Fig. 8a), which is a common indicator of the transtensional regime (Keiding et al., 2009). On the other hand, the exchange of the maximum compression (Fig. 8a, green circle) and the maximum extension (Fig. 8a, black plus sign) in the vertical direction (visible for normal and reverse mechanisms 2 and 4) reflects local stress changes due to over-pressurized fluids.

7. Conclusions

The analysis of the 2017 seismic swarm in the Fagradalsfjall volcano-tectonic segment provides detailed spatiotemporal mapping of the stress field in the vicinity of an aseismic dike. The tectonic stress is consistent with the regional tectonic setting; however, it shows local variations of the stress around the dike. This finding is extremely relevant, since the 2017 seismic activity preceded subsequent much larger activity in 2021, which finally led to the strong Fagradalsfjall volcanic eruption on March 19, 2021 at the same place.

The detected stress field was strongly heterogeneous with different stress regimes manifested by a mix of shear, tensile and compressive fracturing. Though the fracturing was diverse, the orientations of the principal stress coordinate system was stable and consistent with the regional transtensional setting at the Reykjanes Peninsula. The most remarkable feature of the stress inversion was the stable direction of σ_1 and σ_3. The most prominent direction is in the azimuth of $120° \pm 8°$ and represents the overall extension related to rifting (σ_3 axis). It was reported also by Keiding et al. (2009) and supported by geodetic strain directions (Keiding et al., 2008).

The evolution of stress in space and time mapped its local changes. Instead of a gradual and smooth rotation within the focal zone, the stress axes abruptly switched their directions in the individual stress domains: e.g., σ_3 became σ_1 and/or σ_2 became σ_3. Such a switching of the principal axes originated in fluid escapes and processes related to crustal weakening around the dike. They respond to the initial stages of rifting with the following scenario:

- The gradually increased stress triggered the 2017 activity in the east and activated predominantly shear earthquakes aligned along the transform fault zone (shear faulting in cluster 1 with the strongest M_L 3.7 event). These events accommodated the transform part of the motion along the transtensional plate boundary.
- Next, a subsequent collapse of the uppermost layers occurred just above and around the dike in the direction of the maximum extensive stress Shmin (normal faulting with dip-slips in cluster 2) with the accommodation of tensile motion. The tensile fracturing was associated with normal dip-slips and corresponds to the volcanic fissures in the azimuth of 30–35°.
- The activity terminated by the activation of shear-tensile fractures in the west due to release of the over-pressurized fluids (shear-tensile faulting in cluster 3). At depth, the Shmin was rotated clockwise by ~25° to the azimuth of 145° compared to the overall Shmin direction of ~120° ± 8° for the Reykjanes Peninsula. This is likely produced by the interaction of the overall background stress with a local heterogeneity related to the tuya Fagradalsfjall volcano. This is documented by the exchange of the maximum compression and the maximum extension in the vertical direction (visible for normal and reverse mechanisms in clusters 2 and 4) reflecting local stress changes due to the over-pressurized fluids.

The normal fracturing is mainly located above the aseismic dike in the middle of the 2017 swarm. This aseismic dike represents a zone of crustal weakening during the preparatory phase for future eruption, where magma plays rather a passive role during the extension at the divergent plate boundary. This is supported by the presence of the dip-slip earthquakes associated with collapses of the uppermost layers just

above and around the dike. This is also supported by the absence of crustal magma chamber and primitive lava of the Fagradalsfjall 2021 eruption dominated by melts sourced from the uppermost mantle (Halldórsson et al., 2022).

The strongest earthquake M_L 3.7 was activated along the right-lateral N-S trending fault, one of the two principal fault planes optimally oriented for shearing with respect to the detected stress field. The N-S trending faults are newly activated faults and thus can sustain higher stress. The released seismic energy needs to overcome a barrier resulting in the formation of new faults and cracks associated with the strongest earthquakes. The other principal fault plane is associated with the left-lateral oblique plate boundary. This is a mature fault zone filled with fluids (mainly at depth) and close to failure where seismic energy is released by smaller events.

Such results were achieved by precisely located seismicity, by accurately determined seismic moment tensors, and by identifying different stress domains according to the earthquake focal mechanisms. The inversion for stress in non-overlapping stress domains supported by the analysis of non-DC volumetric components proved the importance of differentiating individual stress regimes. Their distinct spatiotemporal character unveiled the interactions, which point to the initial stages of rifting at the transtensional plate boundary. Finally, the analysis proved the potential of seismic data to map the stress field and tectonic processes in such a complex setting.

Supplementary data to this article can be found online at https://doi.org/10.1016/j.tecto.2023.229761.

Credit author statement

The authors declare that they contributed to the paper in the equal way.

Declaration of Competing Interest

The authors declare the following financial interests/personal relationships which may be considered as potential competing interests:

Václav Vavryčuk reports financial support was provided by the Czech Science Foundation. Pavla Hrubcová reports financial support was provided by the Technological Agency of the Czech Republic.

Data availability

Calculated MTs of 389 events and of the most stable 182 events in the 2017 seismicity are freely available at Zenodo repository (https://doi.org/10.5281/zenodo.7683782).

Acknowledgement

References

Andrew, R.E., Gudmundsson, A., 2008. Volcanoes as elastic inclusions: their effects on the propagation of dykes, volcanic fissures, and volcanic zones in Iceland. J. Volcanol. Geotherm. Res. 177, 1045–1054. https://doi.org/10.1016/j.jvolgeores.2008.07.025.

Angelier, J., Slunga, R., Bergerat, F., Stefánsson, R., Homberg, C., 2004. Perturbation of stress and oceanic rift extension across transform faults shown by earthquake focal mechanisms in Iceland. Earth Planet. Sci. Lett. 219, 271–284. https://doi.org/10.1016/S0012-821X(03)00704-0.

Angelier, J., Bergerat, F., Stefánsson, R., Bellou, M., 2008. Seismotectonics of a newly formed transform zone near a hotspot: earthquake mechanisms and regional stress in the South Iceland seismic zone. Tectonophysics 447, 95–116. https://doi.org/10.1016/j.tecto.2006.07.016.

Argus, D.F., Gordon, R.G., Heflin, M.B., Ma, C., Eanes, R.J., Willis, P., Peltier, W.R., Owen, S.E., 2010. The angular velocities of the plates and the velocity of the Earth's Centre from space geodesy. Geophys. J. Int. 18, 1–48. https://doi.org/10.1111/j.1365-246X.2009.04463.x.

Árnadóttir, T., Lund, B., Jiang, W., Geirsson, H., Björnsson, H., Einarsson, P., Sigurdsson, T., 2009. Glacial rebound and plate spreading: results from the first countrywide GPS observations in Iceland. Geophys. J. Int. 177 (2), 691–716. https://doi.org/10.1111/j.1365-246x.2008.04059.x.

Bjarnason, I.Th., Menke, W., Flóvenz, Ó.G., Caress, D., 1993. Tomographic image of the Mid-Atlantic Plate Boundary in southwestern Iceland. J. Geophys. Res. 98 (B4), 6607–6622. https://doi.org/10.1029/92jb02412.

Björnsson, S., Einarsson, P., Tulinius, H., Hjartardóttir, Á.R., 2020. Seismicity of the Reykjanes Peninsula 1971-1976. J. Volcanol. Geotherm. Res. 391, 106369 https://doi.org/10.1016/j.jvolgeores.2018.04.026.

Boyd, O.S., Dreger, D.S., Gritto, R., Garcia, J., 2018. Analysis of seismic moment tensors and in situ stress during Enhanced Geothermal System development at the Geysers geothermal field, California. Geophys. J. Int. 215 (2), 1483–1500. https://doi.org/10.1093/gji/ggy326.

Brander, J.L., Mason, R.G., Calvert, R.W., 1976. Precise distance measurements in Iceland. Tectonophysics 31, 193–206.

Cesca, S., Sen, A.T., Dahm, T., 2014. Seismicity monitoring by cluster analysis of moment tensors. Geophys. J. Int. 196, 1813–1826. https://doi.org/10.1093/gji/ggt492.

Clifton, A.E., Kattenhorn, S.A., 2006. Structural architecture of a highly oblique divergent plate boundary segment. Tectonophysics 419, 27–40. https://doi.org/10.1016/j.tecto.2006.03.016.

Davi, R., Vavryčuk, V., 2012. Seismic network calibration for retrieving accurate moment tensors. Bull. Seism. Soc. Am. 102 (6), 2491–2506. https://doi.org/10.1785/0120110344.

Davi, R., Vavryčuk, V., Charalampidou, E.-M., Kwiatek, G., 2013. Network sensor calibration for retrieving accurate moment tensors of acoustic emissions. Int. J. Rock Mech. Mining Sci. 62, 59–67. https://doi.org/10.1016/j.ijrmms.2013.04.004.

DeMets, R., Gordon, G., Argus, D.F., Stein, S., 1994. Effect of recent revisions to the geomagnetic reversal time scale on estimates of current platemotions. Geophys. Res. Lett. 21, 2191–2194.

DeMets, C., Gordon, R.G., Argus, D.F., 2010. Geologically Current Plate Motions. Geophys. J. Int. 181, 1–80. https://doi.org/10.1111/j.1365-246X.2009.04491.x.

Einarsson, P., 1991. Earthquakes and present-day tectonism in Iceland. Tectonophysics 189, 261–279.

Einarsson, P., 2008. Plate boundaries, rifts and transforms in Iceland. Jokull 58, 35–58.

Einarsson, P., 2015. Mechanisms of Earthquakes in Iceland. In: Beer, M., Patelli, E., Kougioumtzoglou, I.A., Au, S.-K. (Eds.), Encyclopedia of Earthquake Engineering. Springer, Berlin Heidelberg, pp. 1–15. Springer Verlag, Berlin, Heidelberg. https://doi.org/10.1007/978-3-642-36197-5_298-1.

Einarsson, P., Eyjólfsson, V., Hjartardóttir, Á., 2023. Tectonic framework and fault structures in the Fagradalsfjall segment of the Reykjanes Peninsula Oblique Rift, Iceland. Bull. Volcanol. 85 (2), 9. https://doi.org/10.1007/s00445-022-01624-x.

Einarsson, P., Hjartardóttir, Á.R., Imsland, P., Hreinsdóttir, S., 2018. The structure of seismogenic strike-slip faults in the eastern part of the Reykjanes Peninsula oblique rift, SW Iceland. J. Volcanol. Geotherm. 391, 106372 https://doi.org/10.1016/j.jvolgeores.2018.04.029.

Fischer, T., Hrubcová, P., Salama, A., Doubravová, J., Ágústsdóttir, T., Gudnason, E.Á., Horálek, J., Hersir, G.P., 2022. Swarm seismicity illuminates stress transfer prior to the 2021 Fagradalsfjall eruption in Iceland. Earth Planet. Sci. Lett. 594, 117685 https://doi.org/10.1016/j.epsl.2022.117685.

Foulger, G.R., 2006. Older crust underlies Iceland. Geophys. J. Int. 165, 672–676. https://doi.org/10.1111/j.1365-246X.2006.02941.x.

Foulger, G.R., Anderson, D.L., 2005. A cool model for the Iceland hot spot. J. Volcanol. Geotherm. Res. 141, 1–22. https://doi.org/10.1016/j.jvolgeores.2004.10.007.

Foulger, G.R., Doré, T., Emeleus, C.H., Franke, D., Geoffroy, L., Gernigon, L., Hey, R., Holdsworth, R.E., Hole, M., Höskuldsson, Á., Julian, B., Kusznir, N., Martinez, F., McCaffrey, K.J.W., Natland, J.H., Peace, A.L., Petersen, K., Schiffer, C., Stephenson, R., Stoker, M., 2020. The Iceland microcontinent and a continental Greenland-Iceland-Faroe Ridge. Earth Sci. Rev. 206, 102926 https://doi.org/10.1016/j.earscirev.2019.102926.

Foulger, G.R., Gernigon, L., Geoffroy, L., 2021. Icelandia. In: Foulger, G.R., Hamilton, L.C., Jurdy, D.M., Stein, C.A., Howard, K.A., Stein, S. (Eds.), In the Footsteps of Warren B. Hamilton: New Ideas in Earth Science: Geological Society of America Special Paper, 553, pp. 1–12. https://doi.org/10.1130/2021.2553(04).

Green, R.G., White, R.S., Greenfield, T., 2014. Motion in the north Iceland volcanic rift zone accommodated by bookshelf faulting. Nature Geosci. 7 (1), 29–33. https://doi.org/10.1038/ngeo2012.

Gudmundsson, A., 2000. Dynamics of Volcanic Systems in Iceland: Example of Tectonism and Volcanism at Juxtaposed Hot Spot and Mid-Ocean Ridge Systems. Annu. Rev. Earth Planet. Sci. 28, 107–140. https://doi.org/10.1146/annurev.earth.28.1.107.

Gudmundsson, A., 2006. How local stresses control magma-chamber ruptures, dyke injections, and eruptions in composite volcanoes. Earth Sci. Rev. 79, 1–31. https://doi.org/10.1016/j.earscirev.2006.06.006.

Gudmundsson, A., Bergerat, F., Angelier, J., 1996. Off-rift and rift-zone palaeostresses in Northwest Iceland. Tectonophysics 255, 211–228. https://doi.org/10.1016/0040-1951(95)00138-7.

Halldórsson, S.A., Marshall, E.W., Caracciolo, A., et al., 2022. Rapid shifting of a deep magmatic source at Fagradalsfjall volcano, Iceland. Nature 609, 529–534. https://doi.org/10.1038/s41586-022-04981-x.

Hensch, M., Lund, B., Árnadóttir, T., Brandsdóttir, B., 2016. Temporal stress changes associated with the 2008 May 29 M_W 6 earthquake doublet in the western South Iceland Seismic Zone. Geophys. J. Int. 204 (1), 544–554. https://doi.org/10.1093/gji/ggv465.

Hjartardóttir, Á.R., Einarsson, P., Bramham, E., Wright, T.J., 2012. The Krafla fissure swarm, Iceland, and its formation by rifting events. Bull. Volcanol. 74 (9), 2139–2153. https://doi.org/10.1007/s00445-012-0659-0.

Hjartardóttir, Á.R., Einarsson, P., Björgvinsdóttir, S.G., 2016. Fissure swarms and fracture systems within the Western Volcanic Zone, Iceland – Effects of spreading rates. J. Struct. Geol. 91, 39–53. https://doi.org/10.1016/j.jsg.2016.08.007.

Horálek, J., 2013. Reykjanet. International Federation of Digital Seismograph Networks. Dataset/Seismic Network. http://www.fdsn.org/networks/detail/7E_2013/.

Hrubcová, P., Doubravová, J., Vavryčuk, V., 2021. Non-double-couple earthquakes in 2017 swarm in Reykjanes Peninsula, SW Iceland: Sensitive indicator of volcano-tectonic movements at slow-spreading rift. Earth Planet. Sci. Lett. 563, 116875 https://doi.org/10.1016/j.epsl.2021.116875.

Jain, A.K., 2010. Data clustering: 50 years beyond k-means. Pattern Recogn. Lett. 31, 651–666. https://doi.org/10.1016/j.patrec.2009.09.011.

Jakobsdóttir, S.S., 2008. Seismicity in Iceland: 1994–2007. Jökull 58, 75–100.

Jakoubková, H., 2018. Earthquake Swarms in Diverse Tectonic Environments: West Bohemia and Southwest Iceland, Ph.D. thesis.

Keiding, M., Ámadóttir, T., Sturkell, E., Geirsson, H., Lund, B., 2008. Strain accumulation along an oblique plate boundary: the Reykjanes Peninsula, southwest Iceland. Geophys. J. Int. 172, 861–872. https://doi.org/10.1111/j.1365-246X.2007.03655.x.

Keiding, M., Lund, B., Ámadóttir, T., 2009. Earthquakes, stress, and strain along an obliquely divergent plate boundary: Reykjanes Peninsula, southwest Iceland. J. Geophys. Res. 114, B09306. https://doi.org/10.1029/2008JB006253.

Leaney, W.S., 2014. Microseismic Source Inversion in Anisotropic Media. PhD Thesis,. Univ. British Columbia.

Lomax, A., Michelini, A., Curtis, A., 2009. Earthquake Location, Direct, Global-Search Methods. In: Meyers, R.A. (Ed.), Encyclopedia of Complexity and System Science. Springer, New York, NY, pp. 2449–2473. https://doi.org/10.1007/978-3-642-27737-5_150-2. Part 5,.

Lund, B., Townend, J., 2007. Calculating horizontal stress orientations with full or partial knowledge of the tectonic stress tensor. Geophys. J. Int. 170, 1328–1335. https://doi.org/10.1111/j.1365-246X.2007.03468.x.

Martinez, F., Hey, R., Höskuldsson, Á., 2020. Reykjanes Ridge evolution: Effects of plate kinematics, small-scale upper mantle convection and a regional mantle gradient. Earth-Sci. Rev. 206, 102956 https://doi.org/10.1016/j.earscirev.2019.1029.

Menke, W., Levin, V., Sethi, R., 1995. Seismic attenuation in the crust at the mid-Atlantic plate boundary in south-west Iceland. Geophys. J. Int. 122 (1), 175–182. https://doi.org/10.1111/j.1365-246x.1995.tb03545.x.

Michael, A.J., 1984. Determination of stress from slip data: Faults and folds. J. Geophys. Res. 89 (B13) https://doi.org/10.1029/JB089iB13p11517, 11,517-11,526.

Michael, A.J., 1987. Use of focal mechanisms to determine stress: a control study. J. Geophys. Res. 92 (B1), 357–368. https://doi.org/10.1029/JB092iB01p00357.

Plateaux, R., Bergerat, F., Béthoux, N., Villemin, T., Gerbault, M., 2012. Implications of fracturing mechanisms and fluid pressure on earthquakes and fault slip data in the East Iceland rift zone. Tectonophysics 581, 19–34. https://doi.org/10.1016/j.tecto.2012.01.013.

Sella, G.F., Dixon, T.H., Mao, A., 2002. REVEL: a model for recent plate velocities from space geodesy. J. Geophys. Res. 107, B4. https://doi.org/10.1029/2000JB000033.

Sigmundsson, F., Einarsson, P., Bilham, R., Sturkell, E., 1995. Rift-transform kinematics in south Iceland: Deformation from Global Positioning System measurements 1986 to 1992. J. Geophys. Res., Solid Earth. 100 (B4), 6235–6248. https://doi.org/10.1029/95jb00155.

Sigmundsson, F., Einarsson, P., Hjartardóttir, Á.R., Drouin, V., Jónsdóttir, K., Árnadóttir, T., Geirsson, H., Hreinsdóttir, H., Li, S., Ófeigsson, B.G., 2020. Geodynamics of Iceland and the signatures of plate spreading. J. Volcanol. Geotherm. Res. 391, 106436 https://doi.org/10.1016/j.jvolgeores.2018.08.014.

Thordarson, T., Larsen, G., 2007. Volcanism in Iceland in historical time: volcano types, eruption styles and eruptive history. J. Geodyn. 43, 118–152. https://doi.org/10.1016/j.jog.2006.09.005.

Vavryčuk, V., 2011. Principal earthquakes: Theory and observations for the 2008 West Bohemia swarm. Earth Planet. Sci. Lett. 305 (3–4), 290–296. https://doi.org/10.1016/j.epsl.2011.03.002.

Vavryčuk, V., 2014. Iterative joint inversion for stress and fault orientations from focal mechanisms. Geophys. J. Int. 199 (1), 69–77. https://doi.org/10.1093/gji/ggu224.

Vavryčuk, V., 2015a. Earthquake mechanisms and stress field. In: Beer, et al. (Eds.), Encyclopedia of Earthquake Engineering. Springer, Berlin Heidelberg, pp. 728–746 doi: 0.1007/978-3-642-36197-5_288-1.

Vavryčuk, V., 2015b. Moment tensor decompositions revisited. J. Seismol. 19 (1), 231–252. https://doi.org/10.1007/s10950-014-9463-y.

Vavryčuk, V., Adamová, P., 2018. Detection of stress anomaly produced by interaction of compressive fault steps in the West Bohemia swarm region, Czech Republic. Tectonics 37, 4212–4225. https://doi.org/10.1029/2018TC005163.

Vavryčuk, V., Hrubcová, P., 2017. Seismological evidence of fault weakening due to erosion by fluids from observations of intraplate earthquake swarms. J. Geophys. Res. Solid Earth 122, 5, 3701–3718. https://doi.org/10.1002/2017JB013958.

Vavryčuk, V., Bouchaala, F., Fischer, T., 2013. High-resolution fault image from accurate locations and focal mechanisms of the 2008 swarm earthquakes in West Bohemia, Czech Republic. Tectonophysics 590, 189–195. https://doi.org/10.1016/j.tecto.2013.01.025.

Vavryčuk, V., Adamová, P., Doubravová, J., Jakoubková, H., 2017. Moment tensor inversion based on the principal component analysis of waveforms: Method and application to microearthquakes in West Bohemia, Czech Republic. Seismol. Res. Lett. 88 (5) https://doi.org/10.1785/0220170027.

Vavryčuk, V., Adamová, P., Doubravová, J., Ren, Y., 2021. Mapping stress and fluids on faults by nonshear earthquakes. J. Geophys. Res. Solid Earth 126, e2020JB021287. https://doi.org/10.1029/2020JB021287.

Waldhauser, F., Ellsworth, W.L., 2000. A double-difference earthquake location algorithm: method and application to the Northern Hayward fault, California. Bull. Seismol. Soc. Am. 90 (6), 1353–1368. https://doi.org/10.1785/0120000006.

Willemann, R.J., 1993. Cluster analysis of seismic moment tensor orientations. Geophys. J. Int. 115, 617–634.

Yu, Ch., Vavryčuk, V., Adamová, P., Bohnhoff, M., 2018. Moment tensors of induced microearthquakes in The Geysers geothermal reservoir from broadband seismic recordings: Implications for faulting regime, stress tensor and fluid pressure. J. Geophys. Res., Solid Earth 123, 8748–8766. https://doi.org/10.1029/2018JB016251.

Ziegler, M., Rajabi, M., Heidbach, O., Hersir, G.P., Ágústsson, K., Árnadóttir, S., Zang, A., 2016. The stress pattern of Iceland. Tectonophysics 674, 101–113. https://doi.org/10.1016/j.tecto.2016.02.008.

Zoback, M.D., 2007. Reservoir Geomechanics. Cambridge University Press. https://doi.org/10.1017/CBO9780511586477.